

Detection of Quasi-Periodic Oscillations in the Blazar S4 0954+658 with TESS

SHUBHAM KISHORE,^{1,2} ALOK C. GUPTA,^{1,3} AND PAUL J. WIITA⁴

¹*Aryabhata Research Institute of observational sciencES (ARIES), Manora Peak, Nainital 263001, India*

²*Department of Physics, DDU Gorakhpur University, Gorakhpur - 273009, India*

³*Shanghai Frontiers Science Center of Gravitational Wave Detection, 800 Dongchuan Road, Minhang, Shanghai 200240, People's Republic of China*

⁴*Department of Physics, The College of New Jersey, 2000 Pennington Rd., Ewing, NJ 08628-0718, USA*

ABSTRACT

We report the detection of several quasi-periodicities around 0.6–2.5 days in the optical emission of the blazar S4 0954+658. The source was observed by the Transiting Exoplanet Survey Satellite (TESS) in six sectors and it showed these features in all but one of them, with a QPO of 1.52 days apparently present in portions of four of them. We used the generalized Lomb-Scargle periodogram method to search for significant signals and we confirmed them using a weighted wavelet transform for time-frequency domain analyses. We discuss several possible explanations for these rapid quasi-periodic variations and suggest that an origin in the innermost part of the accretion disk is most likely. Within this framework, we provide estimates for the mass of the black hole at the core of this blazar.

1. INTRODUCTION

Active Galactic Nuclei (AGNs) produce tremendous amount of energy across the entire electromagnetic (EM) spectrum that are not traceable to the stars or their remnants. Blazars belong to the fraction of AGNs that are radio-loud and that have their relativistic charged particle jets directed almost along the observer's line of sight ($\leq 10^\circ$) (Urry & Padovani 1995). Blazars are usually classified into two subclasses: BL Lacertae objects (BL Lacs) and flat spectrum radio quasars (FSRQs). BL Lacs show featureless continua or very weak emission lines (i.e., equivalent width (EW) $\leq 5\text{\AA}$) (Stoche et al. 1991; Marcha et al. 1996), whereas FSRQs show prominent emission lines in the composite Optical/UV spectra (Blandford & Rees 1978; Ghisellini et al. 1997). Blazars manifest large flux and spectral variability in all observable EM bands and substantial polarization variability from radio to optical bands, and this emission from blazars is predominantly non-thermal (e.g., Gupta et al. 2019b, and references therein).

The spectral energy distributions (SEDs) of blazars include two broad components (peaks) where the one at lower energy is dominated by synchrotron emission from the relativistic jet and the higher energy one is probably due to the inverse Compton (IC) effect (e.g., Gaur et al. 2010). Considering the recent nomenclature applicable to all types of nonthermal dominated AGNs, based on the position of the lower energy component of the SED, blazars are classified as LSPs (low synchrotron

peaked blazars) if their lower energy component peaks in the near-infrared (NIR) wavelengths ($\nu_{peak} < 10^{14}\text{Hz}$), ISPs (intermediate synchrotron peaked blazars) where the synchrotron emission peaks near the optical energies ($10^{14}\text{ Hz} \leq \nu_{peak} \leq 10^{15}\text{Hz}$), and HSPs (high synchrotron frequency peaked blazars) if their lower energy component peaks in the ultraviolet (UV) or higher energies ($\nu_{peak} \geq 10^{15}\text{ Hz}$) (Abdo et al. 2010).

Quasi-periodic oscillations (QPOs) in the time series data, or light curves (LCs), are frequently detected in X-ray binaries (XRBs) (Remillard & McClintock 2006) but rarely discerned in AGNs (e.g., Gierliński et al. 2008; Gupta 2014, 2018; Gupta et al. 2018; Roy et al. 2022a,b, and references therein). Nonetheless, QPOs have occasionally been claimed to have been in various blazars, narrow line Seyfert 1 (NLS1) galaxies, and other subclasses of AGNs in different EM bands on diverse time-scales as short as a few minutes to as long as a few years (e.g. Gierliński et al. 2008; Espaillat et al. 2008; Gupta et al. 2009, 2018; Lin et al. 2013; Alston et al. 2014, 2015; Gupta 2014, 2018; Ackermann et al. 2015; Pan et al. 2016; Sandrinelli et al. 2016, 2018; Zhang et al. 2017b,a, 2018; Bhatta 2017, 2019; Sarkar et al. 2020, 2021; Tripathi et al. 2021; Roy et al. 2022a,b, and references therein).

The blazar S4 0954+658 ($\alpha_{2000.0} = 09^h58^m47.244^s$, $\delta_{2000.0} = +65^\circ33'54.8''$), situated at a redshift of 0.3694 ± 0.0011 (Becerra González et al. 2021), is usually

classified as a BL Lac object due to the small equivalent width of the emission lines in its spectrum (Stickel et al. 1991); however, this gamma-ray emitter is probably better considered to be a transitional blazar, one falling between the FSRQ and BL Lac categories (Becerra González et al. 2021). This source shows a one-sided radio jet with a polarized hotspot and the polarization of the inner part of the jet indicates a longitudinal magnetic field (Kollgaard et al. 1992). Ghisellini et al. (2011) classified this object as an LBL (low energy peaked BL Lac – same as LSPs) based on the SED. But based on the kinematic features of the radio jet Hervet et al. (2016) classified this source as being in their kinematic class II, which is mostly composed of FSRQs; thus S4 0954+658 can well be understood as a transitional object.

Observations with the MAGIC telescopes led to the first detection of S4 0954+658 at very high energy (VHE) γ -rays in which monitoring of the optical polarization angle revealed a rotation of approximately 100° (MAGIC Collaboration et al. 2018). Bachev (2015) carried out multi-band optical photometric observations of S4 0954+658 in February 2015 when the source displayed an unprecedentedly high optical flux state, and found clear variations on time-scales of minutes, reaching flux changes of $0.1 - 0.2 \text{ mag h}^{-1}$. A multi-color photometric and polarization analysis was done by Hagen-Thorn et al. (2015) in which the color variability was explained by the superposition of a red component and a bluer variable component with a constant relative SED. Optical variability detected by Wagner et al. (1993) showed a large amplitude variation of the order of 100% on the time-scale of a day. Raiteri et al. (1999) too found large amplitude intra-night variations in optical and radio bands, and that a high optical state in the SED is associated with a low radio state and vice versa. They showed that this could be fitted by a steady-emission helical-jet model that points to the variations being a geometrical effect (involving a changing jet orientation with respect to the observer’s line of sight). A possible radio-optical correlation was claimed by Wagner et al. (1993), but this was based on sparsely sampled radio data during an optical outburst phase. Recently Raiteri et al. (2021) also found a possible 3 week time lag between flux variations in radio and optical bands.

Raiteri et al. (2021) carried out a multi-wavelength observational campaign of S4 0954+658 during 2019 July 18 to 2020 July 18 using the Whole Earth Blazar

Telescope (WEBT)¹. Using optical R-band data from WEBT and early Transiting Exoplanet Survey Satellite (TESS)² observations for this source from sectors 14, 20, and 21, they found a quasi-periodicity of 31.2 days that could be caused by the rotation of an inhomogeneous helical jet whose pitch angle varies in time.

In 2008, we started a long-term project to look for QPOs in blazars and NLS1 galaxies in multiple EM bands on different time-scales. In our 1.5 decades long extensive search, we detected only a few occasional QPOs in blazars (e.g., Gupta et al. 2009, 2019a; Lachowicz et al. 2009; Rani et al. 2009, 2010; Kushwaha et al. 2020; Sarkar et al. 2020, 2021; Tripathi et al. 2021; Roy et al. 2022a,b) and in a NLS1 (e.g., Gupta et al. 2018) in different EM bands on diverse time-scales. It appears that detectable QPOs in blazars and NLS1 galaxies are quite rare and somewhat difficult to be explained within existing AGN emission models. Here we present a search for optical QPOs in the blazar S4 0954+658 using data taken for the source by TESS throughout its entire period of operation up to January 27, 2022.

The paper is arranged as follows. In Section 2, we summarize basic information about the TESS satellite and its instrument. In Section 3, we present the TESS observations of the blazar S4 0954+658 and our reduction technique for this data. In Section 4, we briefly describe various analysis techniques we have used in search for QPOs. In Section 5, we give the results of those analyses, indicating the presence of a rather persistent QPO. A discussion and conclusions are in Section 6.

2. INSTRUMENT PARTICULARS

Employing its four wide-field optical charge-coupled device (CCD) cameras to track at least 200,000 main-sequence dwarf stars to search for exoplanetary transits (Ricker et al. 2014), TESS had a goal of 50 parts per million (ppm) photometric precision on stars with broad band (Ricker et al. 2014) TESS magnitudes 9–15, although it can also provide extremely useful data on fainter astronomical objects. TESS measures the brightness of preselected target objects every 2 minutes. As the observations for these targets are done, they are read out as “postage stamps” and are made available to the community as target pixel files (TPFs) and calibrated LC files. In addition, TESS records the full frame im-

¹ <https://www.oato.inaf.it/blazars/webt/>

² <http://tess.gsfc.nasa.gov>

ages (FFIs) every 30 minutes (Ricker et al. 2014). These FFIs enable users to conduct photometry on any target within the $24^\circ \times 96^\circ$ field-of-view (FOV).

Table 1. TESS instrument details.

Single camera FOV	$24^\circ \times 24^\circ$
Combined FOV	$24^\circ \times 96^\circ$
Entrance pupil diameter	10.5 cm
Focal ratio	f/1.4
Wavelength range	600–1000 nm
Ensquared energy	50% within $15 \times 15 \mu\text{m}$ (1 pix ²) 90% within $60 \times 60 \mu\text{m}$ (4 pix ²)

With a resolution of 21 arcseconds/pixel, the TESS satellite’s four cameras each have a FOV of $24^\circ \times 24^\circ$ and they are attached in a row, thereby constituting the total FOV of $24^\circ \times 96^\circ$. Initially, the whole sky was divided into 26 strips, called ‘sectors’ (leaving some gaps near the equatorial region), for its sector-wise supervision. However, subsequent re-observations of essentially the same portions of the sky commenced when the 2 years tenure of the primary mission was completed; this increased the number of enumerated sectors. Because of the rectangular FOV, there are certain regions in the sky that lie in several sectors (especially near the polar regions). TESS’s detailed instrumental specifications are online.³

3. OBSERVATIONS AND DATA REDUCTION Goodness Metrics vs. L2-Norm Penalty (α)

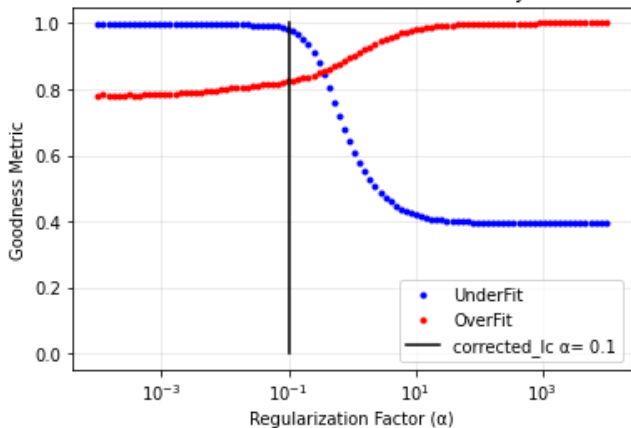


Figure 1. Goodness metric scan plot for the source 0954+658 observed in sector 14.

After observing a sector for roughly 27 days, TESS creates a targetpixelfile of the preselected source that consists of a series of images taken at a cadence of 2 minutes.

Although an LC can be generated using the targetpixelfile, TESS also creates an LC file that directly gives a nominal LC of the desired object. These 2-min cadence TESS LCs are of two types: simple aperture photometry flux (SAP_FLUX, which is the flux obtained by summing up all the pixel counts in an already defined aperture as a function of time) and pre-search data conditioned simple aperture photometry (PDCSAP_FLUX, which is the SAP flux from which long-term trends have been removed); both are available at Mikulski Archive for Space Telescopes⁴.

Where the SAP_FLUX behaves as raw flux data, a Presearch Data Conditioning (PDC) module used by the TESS science processing operations center (SPOC), gives PDCSAP_FLUX, after executing a few necessary corrections to the SAP_FLUX which include the identification and removal of instrumental characteristics introduced due to focus or pointing changes. PDC also accounts for and eliminates isolated outliers (Jenkins et al. 2016). In short, the PDCSAP_FLUX is a sort of refined LC, that is usually cleaner than the SAP flux and has fewer systematic trends; however, it may not exclude instrumental effects producing phony variability which can be taken care of by subsequent pipelines and it can remove some real longer-term variations present in AGNs. It is important that TESS also gives the quality of each datum taken indicated by quality flags so that poor data can be removed. These quality flags, represented by integers, indicate the types of anomalies detected in the data corresponding to each cadence or image. These integers are considered as individual bits that have the meanings described in Table 32 of Twicken et al. (2020). The quality flag for a good cadence without any anomalies is set to zero. The quality of each cadence in our analysis has been taken care of in our pipeline, and we used only data points after reduction that have quality flags of zero.

We made use of Lightkurve, a Python package for Kepler and TESS data analysis (Lightkurve Collaboration et al. 2018), starting our data reduction with SAP_FLUX. We then used co-trending basis vectors (CBVs, a set of systematic trends present in the ensemble of LC data for each CCD) which include three sets of multi-scale basis vectors, a constant vector and spike vectors, to remove both long term trends and sudden spikes. The CBVs act like models, the SAP_FLUX like inputs, and the resultant LC is the output. While reducing the SAP_FLUX (i.e., fitting the CBVs), there

³ <https://heasarc.gsfc.nasa.gov/docs/tess/the-tess-space-telescope.html>

⁴ <https://mast.stsci.edu/portal/Mashup/Clients/Mast/Portal.html>

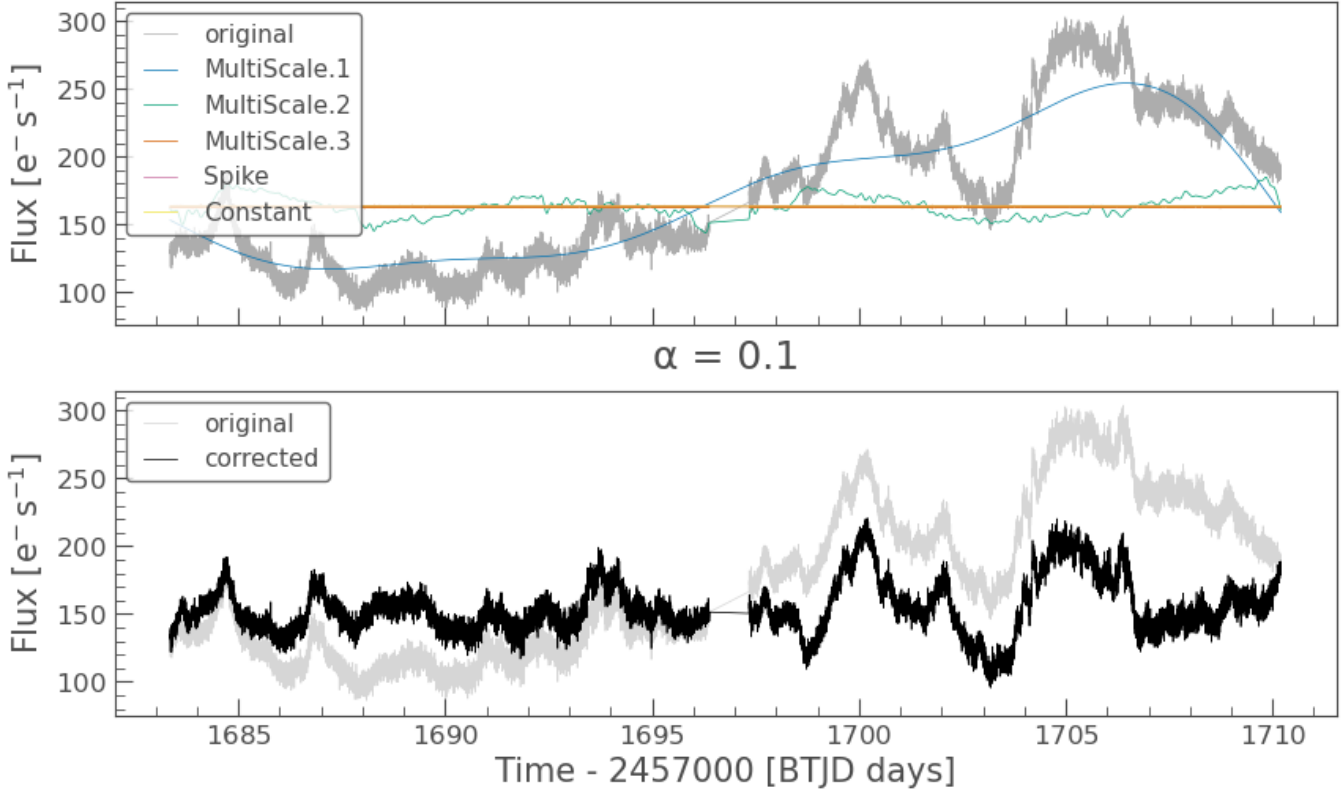


Figure 2. Diagnostic plot for the source 0954+658 observed in sector 14. Upper panel: MultiScale, Spike, and Constant are the different CBVs used for the data reduction. Lower panel: the curve labeled original is the raw flux or the SAP_FLUX, while the Lc after the CBVs and outlier mask are applied is labeled as corrected.

are three parameters that need to be kept in check, viz., underfitting goodness metric, overfitting goodness metric and the regularization parameter (α)⁵. The overfitting metric measures the noise introduced in the light curve after the correction by measuring the broadband power spectrum via a Lomb-Scargle Periodogram both before and after the correction. An increase in this power after the correction indicates over-fitting and noise introduction. The underfitting metric measures the mean residual target-to-target Pearson correlation between the target under study and a selection of neighboring targets. The fitting has been done using L2-Norm/Ridge regression method that includes the third parameter α (the ridge regression coefficient estimates are the values that minimize Eq. 6.5 of James et al. 2013, where α is replaced by λ). Using the goodness metrics as the Loss Function (difference between data and model) and optimizing the Ridge regularization penalty term, a ridge regression produces a set of coefficient estimates for each value of α . The goodness met-

rics are parts of the `lightcurve.correctors.metrics` module, and we have employed them through the `lightcurve.correctors.CBVCorrector` module.

For a good fit, the values of both the underfitting and overfitting goodness metrics should be kept at or above 0.8, and the α should be as low as possible (to make the model fitting a linear regressive). An example of the values of the two goodness metrics and α we used for one TESS sector of the observations of 0954+658 are given in Fig. 1. We have chosen an optimum value, $\alpha = 0.1$. Corresponding to this α , the resulting overfitting and the underfitting metric values found as results of our calibration pipeline are listed in Table 2 for each sector. The resultant LCs, an example of which is shown in Fig. 2, after removing outliers (data points beyond 3σ variance), were then used for the search for any quasi-periodicities.

4. DATA ANALYSIS

4.1. Data Segmentation and Binning

The final LC that is obtained after reduction contains a ~ 1 -day gap in each of the sectors which arise from one of two reasons. One of these is that the satellite

⁵ <http://docs.lightcurve.org/tutorials/2-creating-light-curves/2-3-how-to-use-cbvcorrector.html>

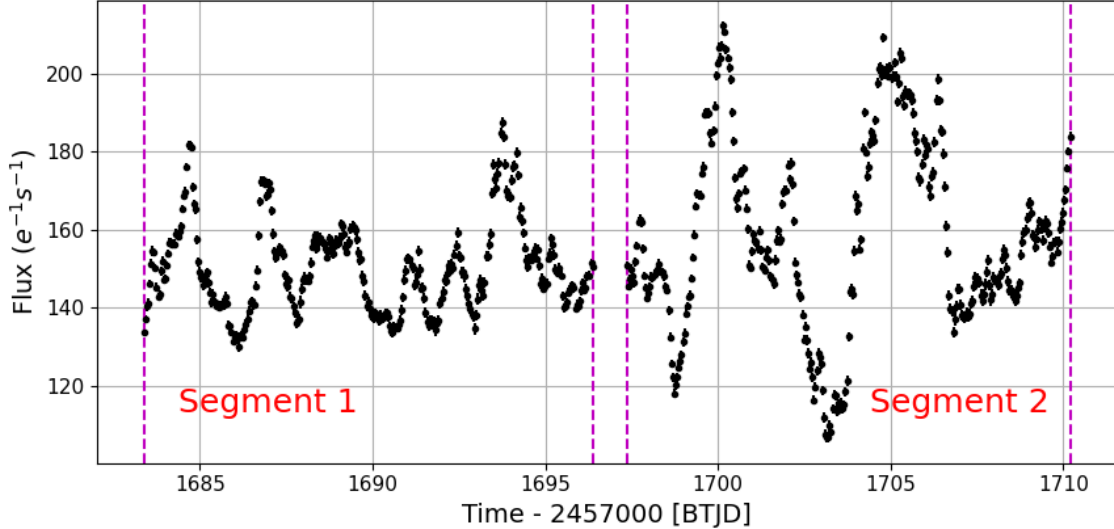


Figure 3. One hour binned reduced LC of 0954+658 observed in sector 14.

Table 2. Flux calibration details

Sector	Overfitting metric	Underfitting metric
14	0.823	0.982
20	0.913	0.993
21	0.833	0.991
40	0.969	0.999
41	0.967	0.998
47	0.908	0.976

is sending the observed data to Earth during that time span. The gap can also be due to the satellite waiting for any commands to be uploaded. This gap creates an uneven sampling in the LC, so the whole LC of one sector is divided into two parts which we call ‘segments’. After segmenting the LC in each sector, we bin the data in 1 hour chunks for their further use in the analysis. Fig. 3 shows this binned LC for Sector 14.

4.2. Generalized Lomb-Scargle Periodogram (GLSP)

The Lomb-Scargle Periodogram (LSP) (Lomb 1976; Scargle 1982) is a method that is used to detect any periodicity in a time series data (even with irregular sampling) and that uses χ^2 statistics to fit sine and cosine functions throughout the time series data. The LSP fits a sinusoidal model to the data at each frequency, with a larger power reflecting a highly possible presence of the frequency. If σ^2 is the variance, the normalized periodogram or GLSP (Horne & Baliunas (1986); [Eq. 13.8.4] of Press et al. (2007)) is given as

$$P(\omega) = \frac{1}{2\sigma^2} [\text{cosine term} + \text{sine term}], \quad (1)$$

where cosine and sine terms are given as

$$\text{cosine term} = \frac{\left[\sum_j (X_j - \bar{X}) \cos \omega(t_j - \tau) \right]^2}{\sum_j \cos^2 \omega(t_j - \tau)}, \quad (2)$$

$$\text{sine term} = \frac{\left[\sum_j (X_j - \bar{X}) \sin \omega(t_j - \tau) \right]^2}{\sum_j \sin^2 \omega(t_j - \tau)}, \quad (3)$$

and where t_j is the time of a measurement, X_j the corresponding flux value, \bar{X} is the mean of X_j , ω is the frequency, and τ is given through

$$\tan(2\omega\tau) = \frac{\sum_j \sin(2\omega t_j)}{\sum_j \cos(2\omega t_j)}. \quad (4)$$

4.3. Wavelet Analysis

Fourier analysis provides an ideal tool to detect a periodic or quasi-periodic fluctuation, as long as the fluctuation is present with constant amplitude and constant phase. But astronomical systems do not generally show this constancy and any periodic episode often appears transiently. Hence Fourier analysis may not be optimal where signals may exhibit short intervals of characteristic oscillation. As an alternative approach that can focus its attention on a short and limited time span of the data, the Wavelet Transform method is well-suited to detect transient periodic fluctuations. It can allow for examination of any time evolution of the parameters (period, amplitude, phase) describing periodic and quasi-periodic signals.

A Wavelet is a wave-like oscillation that is localized in time. Wavelets have two basic properties: scale and location. Scale (or dilation) defines how “stretched”

or “squished” a wavelet is. Location defines where the wavelet is positioned in time. Following the python code based on a method given by Foster (1996), we employed the Weighted Wavelet Z (WWZ)-transform using a Morlet wavelet as a mother wavelet. This is given as $f(z) = e^{-cz^2}(e^{iz} - e^{-1/4c})$ with $z = \omega(t - \tau)$, where c tells how quickly the wavelet decays and is chosen usually, so that the exponential term decreases significantly in a single cycle viz. $2\pi/\omega$, where ω and τ are scale factor and time shift respectively. A proper choice of c for variable lightcurves is less than $1/8\pi^2$ (Foster 1996). We have chosen $c = 0.001$ for our wavelet analysis because such small values of c make the constant $e^{-1/4c}$ essentially negligible and the Morlet wavelet reduces to

$$f(z) = e^{-cz^2+iz}. \quad (5)$$

Then the WWZ map that is created using convolution of the LC and the wavelet (scale factor and time-shift dependent) containing the data decomposed in time and frequency domain is given as

$$W[\omega, \tau; x(t_\alpha)] = \omega^{1/2} \sum_{\alpha=1}^N x(t_\alpha) f^*[\omega(t_\alpha - \tau)]. \quad (6)$$

Eq. (6) is essentially similar to a windowed Fourier transform, with window $e^{-c\omega^2(t-\tau)^2}$. The end result is a two-dimensional plot showing amount of power as a function of both period (or frequency) and time. Detailed information on the WWZ can be found in Foster (1996) and Templeton (2004).

4.4. LC simulation and Peak Significance

To inspect the significance of any peculiar peak obtained in the GLSP and WWZ of LC in any particular segment, simulations using Monte Carlo method were done to create artificial LCs using the parameters calculated after fitting the Power Spectral Density (PSD) of the same segment’s LC. We followed the method given in Emmanoulopoulos et al. (2013) in which firstly, the PSD of the segment’s LC was fitted with a power-law distribution $P(\nu) = A\nu^{-\alpha}$ where P is the power at frequency ν with normalization constant A and spectral index α , and using these two parameters (A & α) obtained from the fit, 5000 individual LCs were generated using a Monte Carlo simulation for each segment. The power law fit values are listed in Table 3. The spectral indices of the source in different segments here lie in the range between 1.43 and 2.41 having a mean of 1.96 ± 0.28 that is quite typical for the optical variability of blazars (Carini et al. 2020). The normalization constants, however, have a somewhat wider range. A GLSP for each of these pseudo-LCs was then obtained individually. With

that large number of GLSPs at each frequency, the mean GLSP with its standard deviation was used to estimate the significance of any peaks.

Table 3. PSD fit parameters for each segment

Sector	Segment	Spectral index (α)	Normalization constant (A)
14	1	2.13	1.1×10^{-5}
	2	2.12	2.4×10^{-5}
20	1	1.94	2.3×10^{-5}
	2	2.15	1.4×10^{-5}
21	1	1.71	2.5×10^{-5}
	2	1.43	2.2×10^{-4}
40	1	1.71	2.0×10^{-5}
	2	2.00	1.2×10^{-5}
41	1	1.90	1.1×10^{-5}
	2	1.67	3.5×10^{-5}
47	1	2.37	1.5×10^{-5}
	2	2.41	0.8×10^{-5}

5. RESULTS

In this work, we have collected and analyzed the data for S4 0954+658 from TESS, which observed it in a total of 6 sectors (14, 20, 21, 40, 41 & 47) until now. We divided them into a total of 12 segments because as described in Sect. 4.1], a gap of roughly one day was present at the center of each sector. We present here the results of our analyses of these segments, and start with the first one, Sector 14, Segment 1. To detect any periodicity, we first used the GLSP and to check the results of our GLSP analysis, we then performed the WWZ analysis that gives the power as a function of time and frequency. From this WWZ map, a time averaged periodogram (TAP), or mean of the WWZ, was obtained. The GLSP and the TAP for this segment have been plotted simultaneously in the lower right panel of Fig. 4b to allow for a comparison of their normalizations and peaks.

To find the significance level, we followed the method described in Sect. 4.4 and found different possible QPOs at various significance levels for different Segments. We quote significance levels of any particular frequency only if the GLSP peak and TAP peak corresponding to that frequency both touch or cross the 4σ level. We provide the results of these analyses in Table 4 and discuss each segment briefly below.

Table 4. Segment-wise significant peaks, corresponding periods and their significances

Sector	Segment	Peak Frequency (day ⁻¹)	Period (days)	LSP Significance level (σ)	TAP significance level (σ)
14	1	0.43	2.33	8.6	12.0
		0.74	1.35	11.6	11.6
20	1	0.20	5.00	4.2	11.6
		0.65	1.54	10.0	11.3
21	1	0.90	1.11	5.7	5.0
		0.36	2.78	4.5	6.3
		0.61	1.64	6.1	6.4
		0.73	1.37	9.4	9.2
21	2	0.92	1.09	5.8	5.3
		–	–	–	–
		–	–	–	–
		–	–	–	–
40	1	0.33	3.03	6.8	12.1
		0.65	1.54	6.1	5.7
		0.72	1.39	5.7	4.1
		0.83	1.20	10.7	7.6
41	1	0.56	1.79	6.3	8.0
		0.66	1.52	10.3	13.3
47	1	0.23	4.35	4.6	9.2
		0.80	1.25	8.6	6.5
		0.50	2.00	10.9	12.7
		0.66	1.52	17.5	18.9
		1.00	1.00	13.0	10.4
		1.13	0.88	16.6	12.9
47	2	1.49	0.67	22.2	12.6
		1.69	0.59	26.6	13.5
		–	–	–	–

5.1. Sector 14

Segment 1—Visual inspection of the LC obtained in this segment provides an indication of a probable QPO. The GLSP (Fig. 4a) of this LC shows peaks at multiple frequencies: 0.20 day⁻¹, 0.43 day⁻¹ and 0.74 day⁻¹. The peak at 0.43 day⁻¹ touches the 8.6 σ and the one at 0.74 day⁻¹ touches the 11.6 σ level. These values are confirmed by the TAP obtained from the WWZ (Fig. 4b) method. The corresponding QPO periods are 2.33 days and 1.35 days. The WWZ plot indicates that the 0.43 day⁻¹ signal weakens somewhat during the course of this observation but remains clearly visible throughout the time span, while the one at 0.74 day⁻¹ undergoes a gradual rise in strength, followed by a decline, and is most visible for ~ 7 days corresponding to over 5 cycles during this segment. Although there

is a good amount of power also present at 0.20 day⁻¹, it barely touches the 1.5 σ level. In any event, such frequencies are too low to consider further since the corresponding 5 days period would show fewer than 3 cycles which could easily arise by chance from red-noise (Press 1978). When the GLSP is looked upon closely at higher frequencies near 1.8 day⁻¹, we see evidence for two peaks crossing the 4 σ level; however, these putative QPOs have very low powers compared to the noted ones.

Segment 2—The LC of this segment, along with those of other segments considered in this paper are displayed in Fig. 5. The GLSP and the TAP for the LC of this segment, shown in Fig. 6A, both peak at 0.2 day⁻¹. There is a difference in the powers obtained by the two

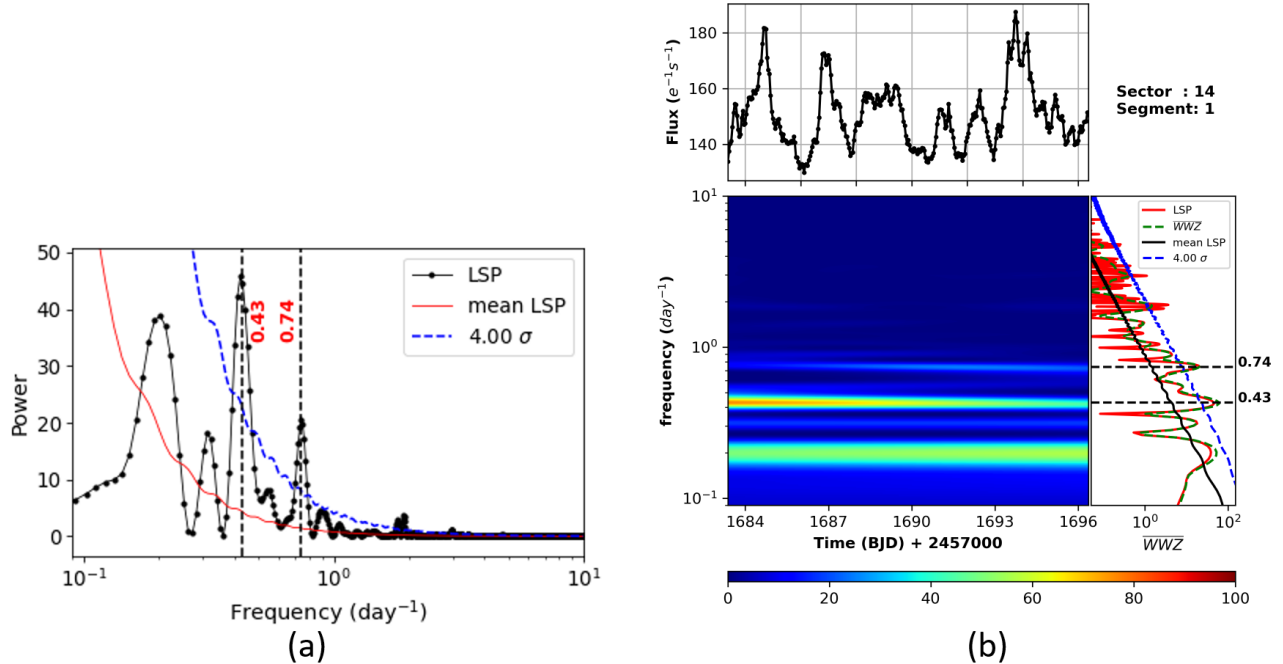


Figure 4. (a) The GLSP of Sector 14 Segment 1 LC. (b) The upper plot is the 1 hour binned LC corresponding to the same segment. The lower left figure is the WWZ transform of this LC, showing the power in time and frequency domains. The lower right panel includes the time-averaged periodogram of the WWZ transform, the GLSP, the mean LSP (GLSP-fit) and the 4σ significance level.

methods, with the GLSP being the weaker one, though both are at or above the 4σ level. The peak has a corresponding period of 5 days spanning the whole segment which, however, as noted above is too long to be taken seriously within a single segment. But given that there was also an indication of such a period in the immediately preceding Segment 1, we can say that there may be a signal there that is present for 5 cycles. Considering this, an additional analysis was performed to inspect this entire sector, but we did not find the frequency peak corresponding to the 5 day period beyond the 4 sigma level.

5.2. Sector 20

Segment 1—The LC shows a great deal of variability that could indicate a possible QPO. Both the GLSP power and the WWZ plot and TAP power shown in Fig. 6B agrees with that assessment and has a peak at 0.65 day^{-1} covering the whole segment except near the very end. Its LSP and TAP peaks have significance levels of 10.0σ and 11.3σ , respectively, corresponding to a period of 1.54 days, so the periodicity spans over 8 cycles. The apparent peak at lower frequencies is not significant. A peak with substantial power is also present at 0.90 day^{-1} , and can be traced throughout the segment, corresponding to the period of 1.11 days.

Segment 2—There are many oscillations in this LC shown that might suggest the presence of a QPO in this segment as well. The results of GLSP and TAP from WWZ shown in Fig. 6C yield various peaks in its periodogram at frequencies: 0.36 days^{-1} , 0.61 days^{-1} , 0.73 days^{-1} and 0.92 days^{-1} , all of which reach a nominal significance level of 4.5σ . The corresponding periodicities are: 2.78 days, 1.64 days, 1.37 days and 1.09 days. However, in that, the strongest signal is at the lowest of those frequencies corresponds to fewer than 5 cycles, while the WWZ plot shows it weakening during the course of this observation, we cannot claim a firm detection. The next two higher frequency putative signals bracket the one seen at 0.65 day^{-1} in Segment 1 of the same sector. These two peaks have a mild presence during the whole segment involving a gradual rise near at the end. In addition, there is another at 0.92 day^{-1} with its weak presence in the second half of the span for ~ 8 days.

5.3. Sector 21

The LCs in both segments in Fig. 5 are definitely variable, but neither hints at a QPO. The GLSP and WWZ plots shown in Figs. (6D, 6E) for Segments 1 and 2, respectively, give no evidence for a signal that could go beyond a 4σ significance level, and we conclude that there was none at this epoch.

5.4. Sector 40

Segment 1—The GLSP and TAP powers in Fig. 6F show peaks providing evidence of a QPO at frequency 0.33 day^{-1} present throughout the segment at 6.8σ and 12.1σ levels with its apparent harmonic at 0.65 day^{-1} also showing up quite strongly. The corresponding periods are 3.03 days and 1.54 days, so again we cannot give full credence to the former as it would encompass only 4 cycles. However, the latter is more trustworthy and is interestingly close to the signals present in both segments of Sector 20, here with power decaying toward the end of the segment.

Segment 2—The GLSP and the TAP obtained from the WWZ have peaks shown in Fig. 6G at 0.72 day^{-1} at 5.7σ and 4.1σ levels, or 1.39 days, and 0.83 day^{-1} at 10.7σ and 7.6σ levels with a corresponding period of 1.20 days. However, these peaks have lower power, but higher significance, compared to another peak at $\sim 0.20 \text{ day}^{-1}$, but its low nominal significance and such a long period imply that it cannot be taken seriously. Still, it is worth noting that this peak is also apparent in Segment 1 of the same sector.

5.5. Sector 41

Segment 1—The LC shows significant fluctuations with a hint of periodicity. In Fig. 6H, showing the GLSP, WWZ and its TAP, we observe a smeared signal centered at 0.56 d^{-1} , with a corresponding period of 1.79 days at 6.3σ and 8.0σ significance levels in GLSP and TAP, respectively. The WWZ plot indicates that this QPO gains strength after ~ 2 days from the beginning of this epoch and is present until its end, so for over 6 cycles. Another peak with a similar power level appears at $\sim 0.35 \text{ day}^{-1}$ but with a lower significance. This signal, however, is mostly present in the former part of the time domain, and then gradually fades.

Segment 2—In Fig. 6I we see that there is a signal at the same frequency seen in two previous Segments, 0.66 day^{-1} with period 1.52 days, reaching a significance levels of 10.3σ and 13.3σ respectively, in its GLSP and TAP. This peak emerges early in this portion of the observations and then remains strong for the entire segment. We also note that the less significant peak of Segment 1 of the same sector may have reappeared in this segment, but again with low significance.

5.6. Sector 47

Segment 1—Variations in this LC are strong, but provide no obvious signs of QPOs. Nonetheless, two peaks are seen in Fig. 6J to rise above the 4.0σ significance level, at frequencies of 0.23 day^{-1} with appreciable

GLSP and TAP powers and of 0.80 day^{-1} with not very high powers. Again, the longer period corresponding to 0.23 day^{-1} does not meet our criteria for its validation. The period for 0.80 day^{-1} or 1.25 days is thus the most likely QPO during this epoch, and it is present throughout the whole segment.

Segment 2—The LC analysis of this segment is particularly interesting. As seen in Fig. 6K, there are several peaks with substantial and significant powers found in this segment. Two peaks at frequencies 0.50 day^{-1} and 0.66 day^{-1} have the greatest powers and cross the 10σ significance level for both the GLSP and TAP analyses. In addition to these frequency peaks, there are other peaks as well at frequencies: 1.00 day^{-1} , 1.13 day^{-1} , 1.49 day^{-1} and 1.69 day^{-1} . These frequency peaks happen to be rough multiples of the former two frequency peaks, indicating the likely presence of higher-order harmonics of two simultaneously significant peaks. Though the periodicities at 0.50 day^{-1} and 0.66 day^{-1} persist throughout the segment, the rest of the peaks appear and disappear during the segment. We note that the 0.66 day^{-1} QPO has the same frequency as seen in several other segments.

5.7. Black hole mass estimation

Along with its spin and charge, one of the most important quantities of any black hole (BH) is its mass and there are several methods used to estimate the central BH mass (e.g., Peterson & Wandel 2000; McLure & Dunlop 2002; Liang & Liu 2003; Pian et al. 2005; Grier et al. 2013). These methods for the BH mass estimation all require either measurement of spectral lines and/or the bolometric luminosity. Because spectral lines are absent in this source, and we lack its bolometric luminosity during our analysis, we have followed the method described in Gupta et al. (2009) to put limits on the SMBH mass for our source under the assumption that the accretion disk around the SMBH is ultimately responsible for the observed QPO periods. The limited range (~ 0.6 –3 days) of periodic time-scales obtained in all the segments imply that these variations probably originate in the same general region. The minimum QPO time-scale found from our results can be used to estimate the mass of the central BH within the range spanned by a spinless BH (Schwarzschild metric, $a = 0$) and a very rapidly spinning BH (Kerr metric, $a = 0.9982$).

If the period is assumed to be related to the orbital time-scale of some blob or flare near the inner region of the accretion disk (e.g. Zhang & Bao 1991) then using

Eq. (4) of [Gupta et al. \(2009\)](#) the mass, M , of the SMBH is given by

$$\frac{M}{M_{\odot}} = \frac{3.23 \times 10^4 P}{(r^{3/2} + a)(1 + z)}, \quad (7)$$

where M_{\odot} is the sun's mass, P is the observed period in seconds, r is the radial distance, set to the last innermost stable circular orbit (ISCO), in units of GM/c^2 . Using the minimum time-scale of 0.59 days (peak frequency at 1.69 day^{-1} from Sector 47 Segment 2) this leads to an SMBH mass of $(8.22 \pm 0.16) \times 10^7 M_{\odot}$ for a Schwarzschild BH and $(5.22 \pm 0.10) \times 10^8 M_{\odot}$ for a Kerr BH, but it is possible that some emissions arise at distances within the last stable orbit (e.g. [Abramowicz & Nobili 1982](#)). Considering how often the period of 1.52 d is present, it is more likely to pertain to the ISCO. Taking this into account, we suggest that within this framework, more probable BH masses are $(2.12 \pm 0.06) \times 10^8 M_{\odot}$ for a Schwarzschild BH and $(1.35 \pm 0.04 \times 10^9 M_{\odot})$ for a Kerr BH.

6. DISCUSSION & CONCLUSION

In this work, we present the most extensive search for optical QPOs in multiple high cadence and evenly sampled datasets collected from the TESS satellite for the blazar S4 0954+658. The data presented here include all measurements made from the launch of TESS through Jan 2022. We have done a segment-wise analysis (described in Sect. 4.1) of the 6 different sector LCs of S4 0954+658. The results are summarized in Table 4. We have found multiple QPOs in various sectors with differing periodicities. The period of the QPOs that we found mainly lie within the range of 1 – 3 days. Hints of both longer periods and occasional indications of shorter period harmonics are also found. We have used both the robust generalized Lomb Scargle periodogram and the complementary method of wavelet analysis for the confirmation of any detected frequency peak. However we did not confirm and cannot further comment on the possible short-time-scale QPO at 0.62 days found by [Raiteri et al. \(2021\)](#) that includes analyses of the first three sectors, however we do find a relatively weak signal of 0.59 days quasi-periodicity that has appreciable significance in the second segment of Sector 47. Our segment-wise analysis of TESS data alone does not allow us to search for the longer period around 31 d suggested by [Raiteri et al. \(2021\)](#) based on composite light curves.

The fact that the frequency $\sim 0.66 \text{ day}^{-1}$ has been found to recur in various segments of the different sectors, means that it might be considered as the dominant

QPO frequency for S4 0954+658. There are peaks at frequencies 1.13 day^{-1} and 1.69 day^{-1} in Segment 2 of Sector 47, which are more precisely the harmonics of 0.56 day^{-1} and not of 0.66 day^{-1} . This suggests that since 0.56 day^{-1} is quite close to 0.66 day^{-1} in frequency space, and both frequency peaks were present at relatively close epochs, we may have observed a transition to the later frequency. The presence of both 0.56 day^{-1} and 0.66 day^{-1} peaks in the WWZ plots of sector 41 also support such a transition between the two frequencies. The mechanism producing QPOs on time-scales of several hours could be of disk origin or could arise from relativistic jets. Possible disk explanations include location change of the dominant disk hotspot, small epicyclic deviations in both vertical and radial directions from exact planar motions within a thin accretion disk, and trapped pulsational modes within a disk (e.g., [Perez et al. 1997](#); [Abramowicz 2005](#); [Espaillat et al. 2008](#), and references therein). It is also possible for them to arise within the jet through a change in its diameter or growth of a kink instability (e.g., [Jorstad et al. 2022](#)).

Several models based on binary SMBH systems (e.g. [Valtonen et al. 2008](#); [Villforth et al. 2010](#); [Ackermann et al. 2015](#)), persistent jet precession and Lense-Thirring precession of accretion discs (e.g. [Stella & Vietri 1998](#); [Romero et al. 2000](#); [Rieger 2004](#); [Liska et al. 2018](#)) have been proposed to explain QPOs in blazars on years-like periods. Since here, we detected QPOs with periods of a few days, we can probably eliminate such models to explain the optical QPOs reported here in the blazar S4 0954+658.

The redshift (z) of the blazar S4 0954+658 as mentioned earlier is 0.3694, so the intrinsic time-scales corresponding to the observed ones are reduced by the factor of $1 + z$ (i.e., 1.3694), hence shifting the source-frame period of variability in the range of 0.43 days to 3.65 days before considering Doppler factors. Although such fast quasi-periodic variations can be produced by dominant turbulent cells, this mechanism is unlikely because of the multiple appearances of similar periodic time-scales ([Wagner et al. 1993](#)). Shock-in-jet models are known to dominate large-scale flares but are unlikely to produce essentially periodic fluctuations on observed time-scales much less than a year ([Wagner & Witzel 1995](#)).

The Doppler factor reported for the source lies in the range $6.1 < \delta < 35$ ([Tanaka et al. 2016](#); [Jorstad et al. 2017](#); [MAGIC Collaboration et al. 2018](#)). So, models involving jet twists or precession and other ways to change the viewing angle combined with the Doppler boosting

factor are also unlikely to provide valid explanations. As noted earlier, their expected source frame time-scales are in years, so even with the maximum reported δ , the observed time-scales might come down to months or so, which are much longer than seen here for S4 0954+658.

However, if these periodic perturbations in the inner part of the disk are advected into the jet so the observed emission comes from a relativistic flow directly affected by those perturbations, then the value of M would require the results obtained from Eq. (7) to be multiplied by δ , (Gupta et al. 2009). Unfortunately the range of published Doppler values for this source is broad (6.1 – 35), but adopting the 1.52 d period as the fundamental one, we obtain the following ranges for the SMBH mass: $(1.3\text{--}7.4) \times 10^9 M_\odot$ for a Schwarzschild BH and $(8.5\text{--}47) \times 10^9 M_\odot$ for an extreme Kerr one. The

extremely high values arising from the combination of high Doppler factors and Kerr metric make them disfavored together.

This paper includes data collected by the TESS mission. Funding for the TESS mission is provided by the NASA Explorer Program. S. Kishore thankfully acknowledges Mr. Abhradeep Roy for his valuable help while learning QPO data analysis techniques. A.C.G. is partially supported by the Ministry of Science and Technology of China (grant No. 2018YFA0404601) and the National Science Foundation of China (grants No. 11621303, 11835009, and 11973033).

Facility: Transiting Exoplanet Survey Satellite (TESS); *Softwares:* lightkurve (Lightkurve Collaboration et al. 2018), DELCgen (Emmanoulopoulos et al. 2013)

REFERENCES

- Abdo, A. A., Ackermann, M., Agudo, I., et al. 2010, ApJ, 716, 30, doi: [10.1088/0004-637X/716/1/30](https://doi.org/10.1088/0004-637X/716/1/30)
- Abramowicz, M. A. 2005, Astronomische Nachrichten, 326, 782, doi: [10.1002/asna.200510413](https://doi.org/10.1002/asna.200510413)
- Abramowicz, M. A., & Nobili, L. 1982, Nature, 300, 506, doi: [10.1038/300506a0](https://doi.org/10.1038/300506a0)
- Ackermann, M., Ajello, M., Albert, A., et al. 2015, ApJL, 813, L41, doi: [10.1088/2041-8205/813/2/L41](https://doi.org/10.1088/2041-8205/813/2/L41)
- Alston, W. N., Markeviciute, J., Kara, E., Fabian, A. C., & Middleton, M. 2014, MNRAS, 445, L16, doi: [10.1093/mnras/1slu127](https://doi.org/10.1093/mnras/1slu127)
- Alston, W. N., Parker, M. L., Markevičiūtė, J., et al. 2015, MNRAS, 449, 467, doi: [10.1093/mnras/stv351](https://doi.org/10.1093/mnras/stv351)
- Bachev, R. 2015, MNRAS, 451, L21, doi: [10.1093/mnras/1slv059](https://doi.org/10.1093/mnras/1slv059)
- Becerra González, J., Acosta-Pulido, J. A., Boschín, W., et al. 2021, MNRAS, 504, 5258, doi: [10.1093/mnras/stab1274](https://doi.org/10.1093/mnras/stab1274)
- Bhatta, G. 2017, ApJ, 847, 7, doi: [10.3847/1538-4357/aa86ed](https://doi.org/10.3847/1538-4357/aa86ed)
- Bhatta, G. 2019, MNRAS, 487, 3990, doi: [10.1093/mnras/stz1482](https://doi.org/10.1093/mnras/stz1482)
- Blandford, R. D., & Rees, M. J. 1978, PhysS, 17, 265, doi: [10.1088/0031-8949/17/3/020](https://doi.org/10.1088/0031-8949/17/3/020)
- Carini, M., Wehrle, A. E., Wiita, P. J., Ward, Z., & Pendleton, K. 2020, ApJ, 903, 134, doi: [10.3847/1538-4357/abbb92](https://doi.org/10.3847/1538-4357/abbb92)
- Emmanoulopoulos, D., McHardy, I. M., & Papadakis, I. E. 2013, MNRAS, 433, 907, doi: [10.1093/mnras/stt764](https://doi.org/10.1093/mnras/stt764)
- Espallat, C., Bregman, J., Hughes, P., & Lloyd-Davies, E. 2008, ApJ, 679, 182, doi: [10.1086/587023](https://doi.org/10.1086/587023)
- Foster, G. 1996, AJ, 112, 1709, doi: [10.1086/118137](https://doi.org/10.1086/118137)
- Gaur, H., Gupta, A. C., Lachowicz, P., & Wiita, P. J. 2010, ApJ, 718, 279, doi: [10.1088/0004-637X/718/1/279](https://doi.org/10.1088/0004-637X/718/1/279)
- Ghisellini, G., Tavecchio, F., Foschini, L., & Ghirlanda, G. 2011, MNRAS, 414, 2674, doi: [10.1111/j.1365-2966.2011.18578.x](https://doi.org/10.1111/j.1365-2966.2011.18578.x)
- Ghisellini, G., Villata, M., Raiteri, C. M., et al. 1997, A&A, 327, 61. <https://arxiv.org/abs/astro-ph/9706254>
- Gierliński, M., Middleton, M., Ward, M., & Done, C. 2008, Nature, 455, 369, doi: [10.1038/nature07277](https://doi.org/10.1038/nature07277)
- Grier, C. J., Martini, P., Watson, L. C., et al. 2013, ApJ, 773, 90, doi: [10.1088/0004-637X/773/2/90](https://doi.org/10.1088/0004-637X/773/2/90)
- Gupta, A. 2018, Galaxies, 6, 1, doi: [10.3390/galaxies6010001](https://doi.org/10.3390/galaxies6010001)
- Gupta, A. C. 2014, Journal of Astrophysics and Astronomy, 35, 307, doi: [10.1007/s12036-014-9219-7](https://doi.org/10.1007/s12036-014-9219-7)
- Gupta, A. C., Srivastava, A. K., & Wiita, P. J. 2009, ApJ, 690, 216, doi: [10.1088/0004-637X/690/1/216](https://doi.org/10.1088/0004-637X/690/1/216)
- Gupta, A. C., Tripathi, A., Wiita, P. J., et al. 2018, A&A, 616, L6, doi: [10.1051/0004-6361/201833629](https://doi.org/10.1051/0004-6361/201833629)
- . 2019a, MNRAS, 484, 5785, doi: [10.1093/mnras/stz395](https://doi.org/10.1093/mnras/stz395)
- Gupta, A. C., Gaur, H., Wiita, P. J., et al. 2019b, AJ, 157, 95, doi: [10.3847/1538-3881/aafe7d](https://doi.org/10.3847/1538-3881/aafe7d)
- Hagen-Thorn, V. A., Larionov, V. M., Arkharov, A. A., et al. 2015, Astronomy Reports, 59, 551, doi: [10.1134/S1063772915050030](https://doi.org/10.1134/S1063772915050030)
- Hervet, O., Boisson, C., & Sol, H. 2016, A&A, 592, A22, doi: [10.1051/0004-6361/201628117](https://doi.org/10.1051/0004-6361/201628117)
- Horne, J. H., & Baliunas, S. L. 1986, ApJ, 302, 757, doi: [10.1086/164037](https://doi.org/10.1086/164037)

- James, G., Witten, D., Hastie, T., & Tibshirani, R. 2013, An introduction to statistical learning (Springer), doi: [10.1007/978-1-4614-7138-7](https://doi.org/10.1007/978-1-4614-7138-7)
- Jenkins, J. M., Twicken, J. D., McCauliff, S., et al. 2016, in Society of Photo-Optical Instrumentation Engineers (SPIE) Conference Series, Vol. 9913, Software and Cyberinfrastructure for Astronomy IV, ed. G. Chiozzi & J. C. Guzman, 99133E, doi: [10.1117/12.2233418](https://doi.org/10.1117/12.2233418)
- Jorstad, S. G., Marscher, A. P., Morozova, D. A., et al. 2017, ApJ, 846, 98, doi: [10.3847/1538-4357/aa8407](https://doi.org/10.3847/1538-4357/aa8407)
- Jorstad, S. G., Marscher, A. P., Raiteri, C. M., et al. 2022, Nature, 609, 265, doi: [10.1038/s41586-022-05038-9](https://doi.org/10.1038/s41586-022-05038-9)
- Kollgaard, R. I., Wardle, J. F. C., Roberts, D. H., & Gabuzda, D. C. 1992, AJ, 104, 1687, doi: [10.1086/116352](https://doi.org/10.1086/116352)
- Kushwaha, P., Sarkar, A., Gupta, A. C., Tripathi, A., & Wiita, P. J. 2020, MNRAS, 499, 653, doi: [10.1093/mnras/staa2899](https://doi.org/10.1093/mnras/staa2899)
- Lachowicz, P., Gupta, A. C., Gaur, H., & Wiita, P. J. 2009, A&A, 506, L17, doi: [10.1051/0004-6361/200913161](https://doi.org/10.1051/0004-6361/200913161)
- Liang, E. W., & Liu, H. T. 2003, MNRAS, 340, 632, doi: [10.1046/j.1365-8711.2003.06327.x](https://doi.org/10.1046/j.1365-8711.2003.06327.x)
- Lightkurve Collaboration, Cardoso, J. V. d. M., Hedges, C., et al. 2018, Lightkurve: Kepler and TESS time series analysis in Python, Astrophysics Source Code Library. <http://ascl.net/1812.013>
- Lin, D., Irwin, J. A., Godet, O., Webb, N. A., & Barret, D. 2013, ApJL, 776, L10, doi: [10.1088/2041-8205/776/1/L10](https://doi.org/10.1088/2041-8205/776/1/L10)
- Liska, M., Hesp, C., Tchekhovskoy, A., et al. 2018, MNRAS, 474, L81, doi: [10.1093/mnrasl/slx174](https://doi.org/10.1093/mnrasl/slx174)
- Lomb, N. R. 1976, Ap&SS, 39, 447, doi: [10.1007/BF00648343](https://doi.org/10.1007/BF00648343)
- MAGIC Collaboration, Ahnen, M. L., Ansoldi, S., et al. 2018, A&A, 617, A30, doi: [10.1051/0004-6361/201832624](https://doi.org/10.1051/0004-6361/201832624)
- Marcha, M. J. M., Browne, I. W. A., Impey, C. D., & Smith, P. S. 1996, MNRAS, 281, 425, doi: [10.1093/mnras/281.2.425](https://doi.org/10.1093/mnras/281.2.425)
- McLure, R. J., & Dunlop, J. S. 2002, MNRAS, 331, 795, doi: [10.1046/j.1365-8711.2002.05236.x](https://doi.org/10.1046/j.1365-8711.2002.05236.x)
- Pan, H.-W., Yuan, W., Yao, S., et al. 2016, ApJL, 819, L19, doi: [10.3847/2041-8205/819/2/L19](https://doi.org/10.3847/2041-8205/819/2/L19)
- Perez, C. A., Silbergleit, A. S., Wagoner, R. V., & Lehr, D. E. 1997, ApJ, 476, 589, doi: [10.1086/303658](https://doi.org/10.1086/303658)
- Peterson, B. M., & Wandel, A. 2000, ApJL, 540, L13, doi: [10.1086/312862](https://doi.org/10.1086/312862)
- Pian, E., Falomo, R., & Treves, A. 2005, MNRAS, 361, 919, doi: [10.1111/j.1365-2966.2005.09216.x](https://doi.org/10.1111/j.1365-2966.2005.09216.x)
- Press, W. H. 1978, Comments on Astrophysics, 7, 103
- Press, W. H., Teukolsky, S. A., Vetterling, W. T., & Flannery, B. P. 2007, Numerical Recipes 3rd Edition: The Art of Scientific Computing, 3rd edn. (USA: Cambridge University Press)
- Raiteri, C. M., Villata, M., Tosti, G., et al. 1999, A&A, 352, 19
- Raiteri, C. M., Villata, M., Larionov, V. M., et al. 2021, MNRAS, 504, 5629, doi: [10.1093/mnras/stab1268](https://doi.org/10.1093/mnras/stab1268)
- Rani, B., Gupta, A. C., Joshi, U. C., Ganesh, S., & Wiita, P. J. 2010, ApJL, 719, L153, doi: [10.1088/2041-8205/719/2/L153](https://doi.org/10.1088/2041-8205/719/2/L153)
- Rani, B., Wiita, P. J., & Gupta, A. C. 2009, ApJ, 696, 2170, doi: [10.1088/0004-637X/696/2/2170](https://doi.org/10.1088/0004-637X/696/2/2170)
- Remillard, R. A., & McClintock, J. E. 2006, ARA&A, 44, 49, doi: [10.1146/annurev.astro.44.051905.092532](https://doi.org/10.1146/annurev.astro.44.051905.092532)
- Ricker, G. R., Winn, J. N., Vanderspek, R., et al. 2014, in Society of Photo-Optical Instrumentation Engineers (SPIE) Conference Series, Vol. 9143, Space Telescopes and Instrumentation 2014: Optical, Infrared, and Millimeter Wave, ed. J. Oschmann, Jacobus M., M. Clampin, G. G. Fazio, & H. A. MacEwen, 914320, doi: [10.1117/12.2063489](https://doi.org/10.1117/12.2063489)
- Rieger, F. M. 2004, ApJL, 615, L5, doi: [10.1086/426018](https://doi.org/10.1086/426018)
- Romero, G. E., Chajet, L., Abraham, Z., & Fan, J. H. 2000, A&A, 360, 57
- Roy, A., Sarkar, A., Chatterjee, A., et al. 2022a, MNRAS, 510, 3641, doi: [10.1093/mnras/stab3701](https://doi.org/10.1093/mnras/stab3701)
- Roy, A., Chitnis, V. R., Gupta, A. C., et al. 2022b, MNRAS, 513, 5238, doi: [10.1093/mnras/stac1287](https://doi.org/10.1093/mnras/stac1287)
- Sandrinelli, A., Covino, S., Dotti, M., & Treves, A. 2016, AJ, 151, 54, doi: [10.3847/0004-6256/151/3/54](https://doi.org/10.3847/0004-6256/151/3/54)
- Sandrinelli, A., Covino, S., Treves, A., et al. 2018, A&A, 615, A118, doi: [10.1051/0004-6361/201732550](https://doi.org/10.1051/0004-6361/201732550)
- Sarkar, A., Gupta, A. C., Chitnis, V. R., & Wiita, P. J. 2021, MNRAS, 501, 50, doi: [10.1093/mnras/staa3211](https://doi.org/10.1093/mnras/staa3211)
- Sarkar, A., Kushwaha, P., Gupta, A. C., Chitnis, V. R., & Wiita, P. J. 2020, A&A, 642, A129, doi: [10.1051/0004-6361/202038052](https://doi.org/10.1051/0004-6361/202038052)
- Scargle, J. D. 1982, ApJ, 263, 835, doi: [10.1086/160554](https://doi.org/10.1086/160554)
- Stella, L., & Vietri, M. 1998, ApJL, 492, L59, doi: [10.1086/311075](https://doi.org/10.1086/311075)
- Stickel, M., Padovani, P., Urry, C. M., Fried, J. W., & Kuehr, H. 1991, ApJ, 374, 431, doi: [10.1086/170133](https://doi.org/10.1086/170133)
- Stocke, J. T., Morris, S. L., Gioia, I. M., et al. 1991, ApJS, 76, 813, doi: [10.1086/191582](https://doi.org/10.1086/191582)
- Tanaka, Y. T., Becerra Gonzalez, J., Itoh, R., et al. 2016, PASJ, 68, 51, doi: [10.1093/pasj/psw049](https://doi.org/10.1093/pasj/psw049)
- Templeton, M. 2004, JAAVSO, 32, 41
- Tripathi, A., Gupta, A. C., Aller, M. F., et al. 2021, MNRAS, 501, 5997, doi: [10.1093/mnras/stab058](https://doi.org/10.1093/mnras/stab058)

- Twicken, J. D., Caldwell, D. A., Jenkins, J. M., et al. 2020,
Urry, C. M., & Padovani, P. 1995, *PASP*, 107, 803,
doi: [10.1086/133630](https://doi.org/10.1086/133630)
- Valtonen, M. J., Lehto, H. J., Nilsson, K., et al. 2008,
Nature, 452, 851, doi: [10.1038/nature06896](https://doi.org/10.1038/nature06896)
- Villforth, C., Nilsson, K., Heidt, J., et al. 2010, *MNRAS*,
402, 2087, doi: [10.1111/j.1365-2966.2009.16133.x](https://doi.org/10.1111/j.1365-2966.2009.16133.x)
- Wagner, S. J., & Witzel, A. 1995, *ARA&A*, 33, 163,
doi: [10.1146/annurev.aa.33.090195.001115](https://doi.org/10.1146/annurev.aa.33.090195.001115)
- Wagner, S. J., Witzel, A., Krichbaum, T. P., et al. 1993,
A&A, 271, 344
- Zhang, P., Zhang, P.-f., Yan, J.-z., Fan, Y.-z., & Liu, Q.-z.
2017a, *ApJ*, 849, 9, doi: [10.3847/1538-4357/aa8d6e](https://doi.org/10.3847/1538-4357/aa8d6e)
- Zhang, P.-F., Yan, D.-H., Zhou, J.-N., et al. 2017b, *ApJ*,
845, 82, doi: [10.3847/1538-4357/aa7ecd](https://doi.org/10.3847/1538-4357/aa7ecd)
- Zhang, P.-f., Zhang, P., Liao, N.-h., et al. 2018, *ApJ*, 853,
193, doi: [10.3847/1538-4357/aaa29a](https://doi.org/10.3847/1538-4357/aaa29a)
- Zhang, X. H., & Bao, G. 1991, *A&A*, 246, 21

SUPPLEMENTARY MATERIALS
SECTOR-WISE BINNED LIGHTCURVES

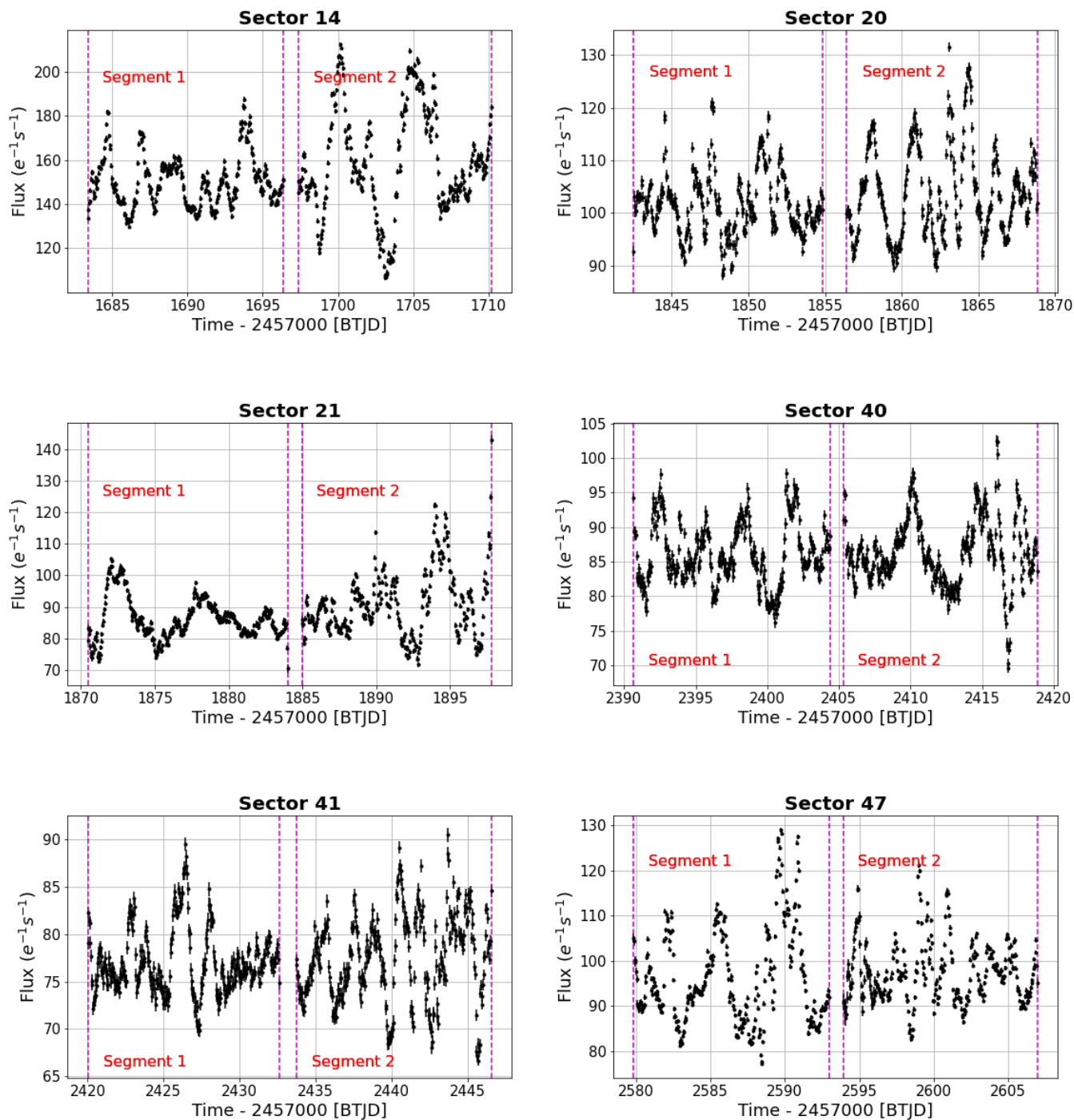


Figure 5. 1 hour binned LCs of S4 0954+658 in all observed sectors.

SEGMENT-WISE GLSP AND WAVELET TRANSFORM IN EACH SECTOR

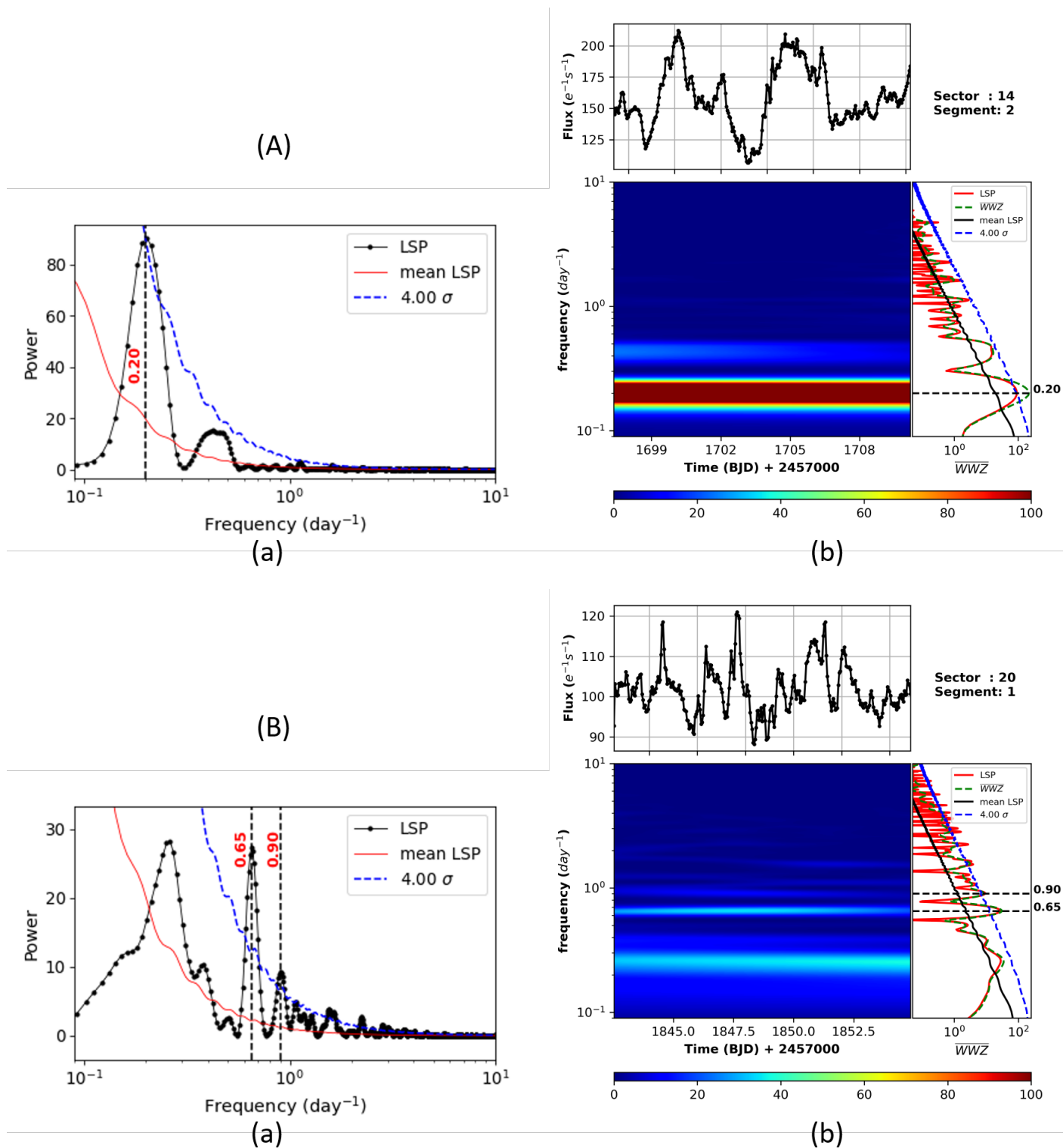
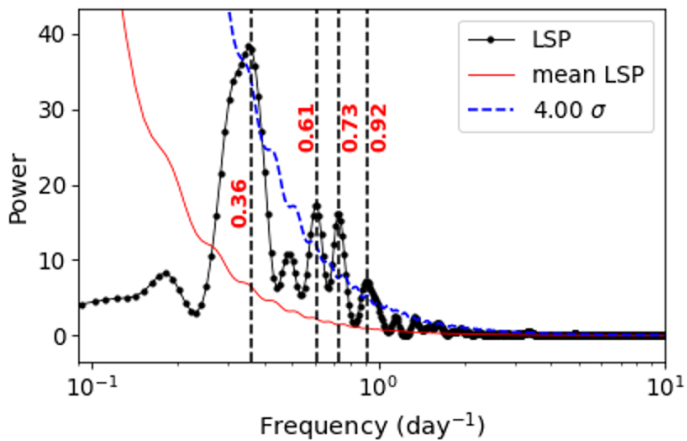
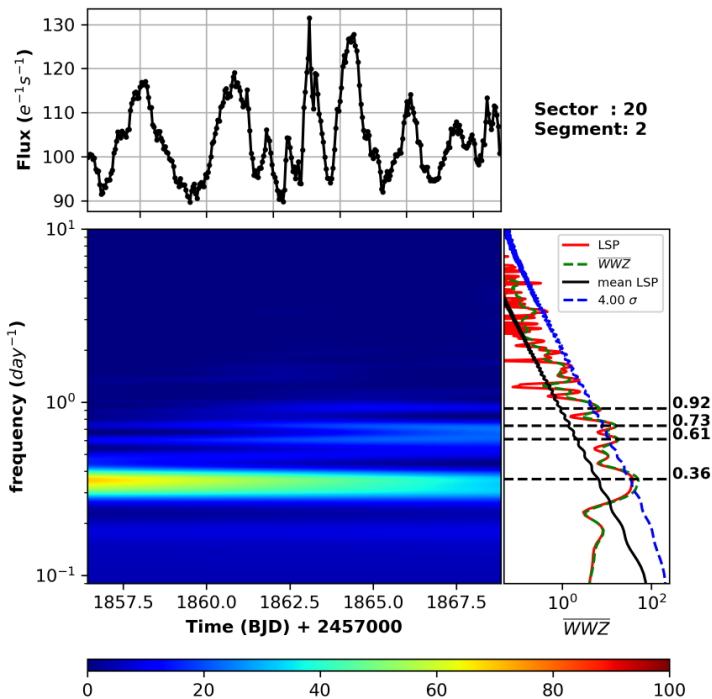


Figure 6. The upper-case letters label the GLSP and WWZ plots for individual segments in each sector, here the second segment for Sector 14 and first for Sector 20. The lower-case letters within each panel denote the same GLSP, binned LC, WWZ, mean powers and 4σ significance level as in Fig. 4.

Fig. 6 continued...

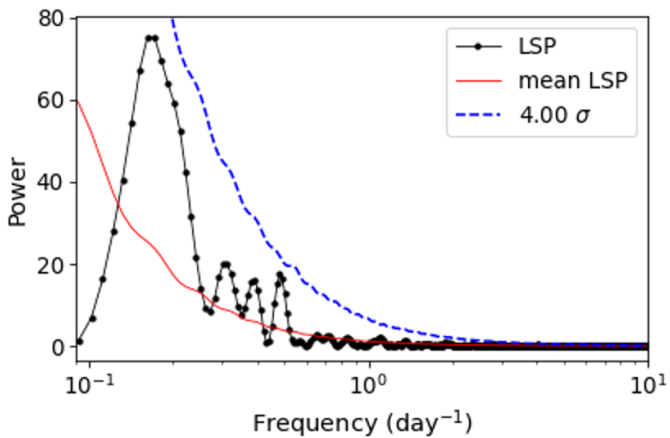
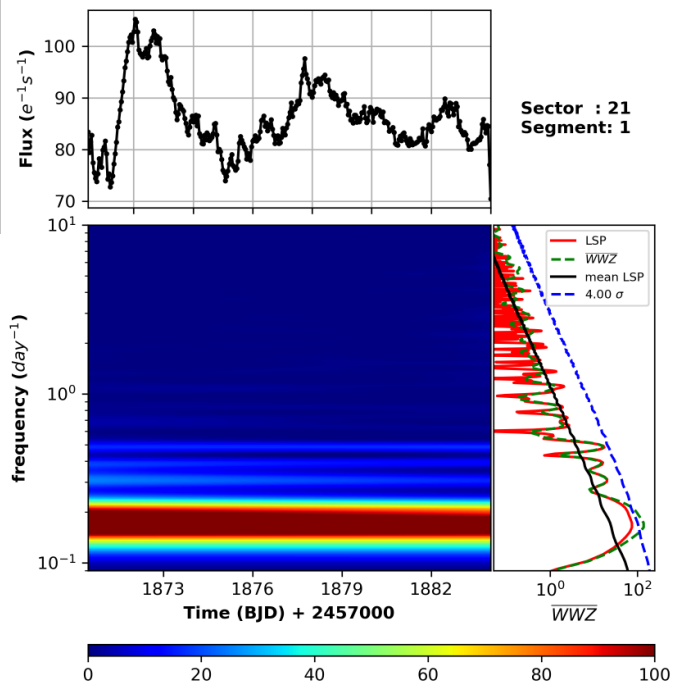
(C)



(a)

(b)

(D)



(a)

(b)

Fig. 6 continued...

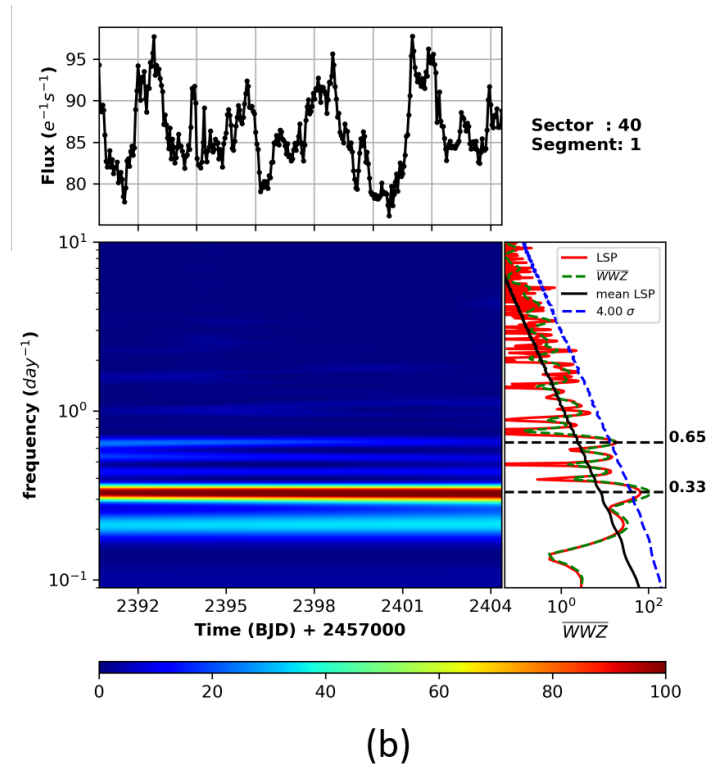
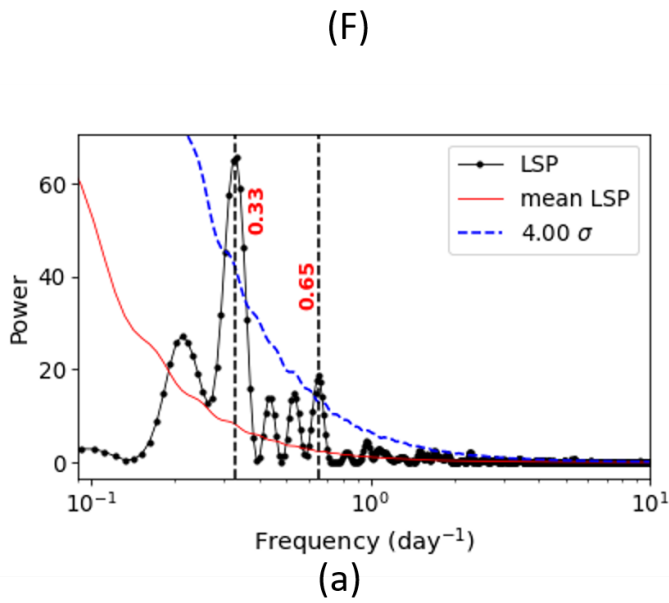
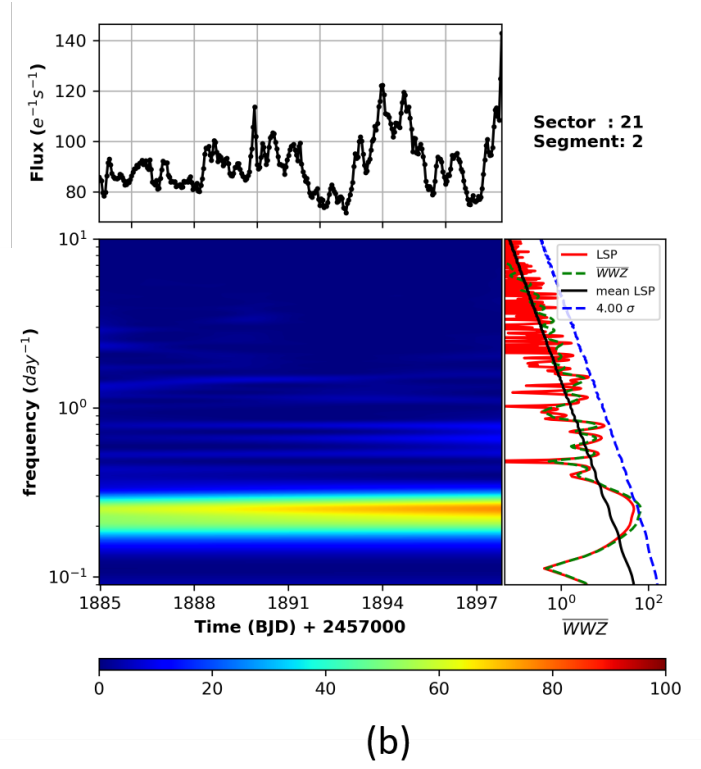
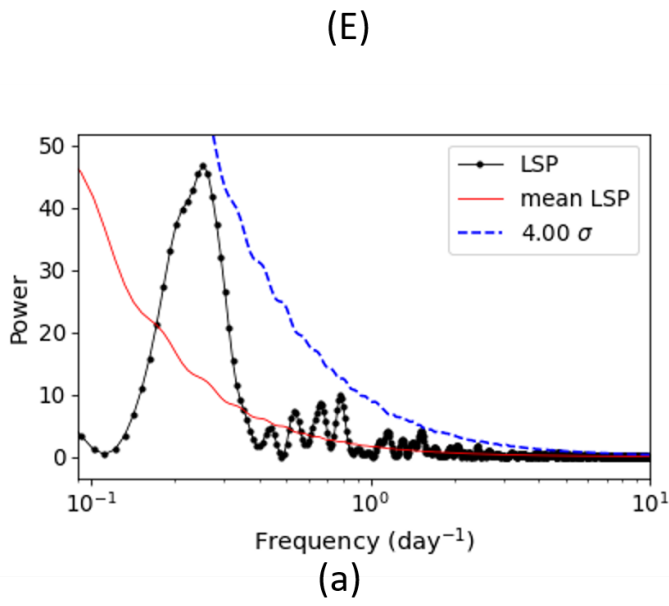
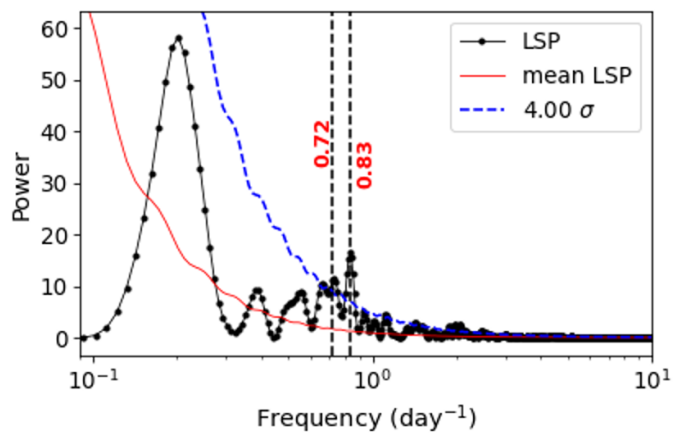
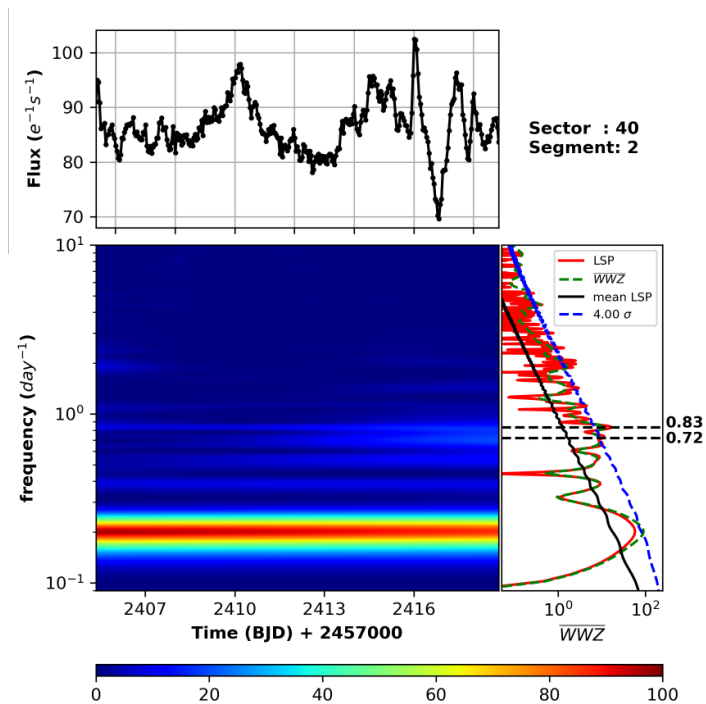


Fig. 6 continued..

(G)

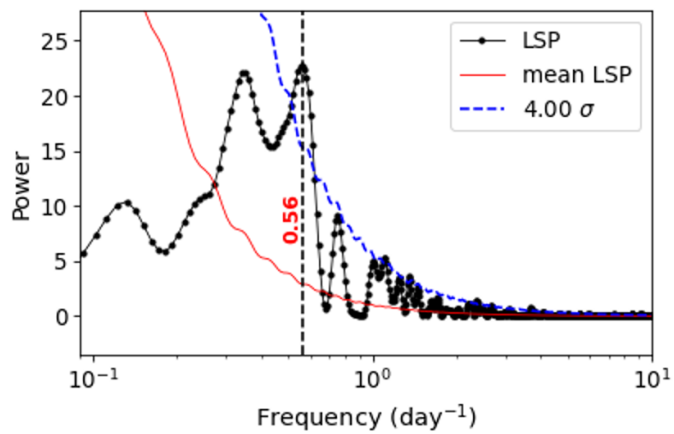


(a)

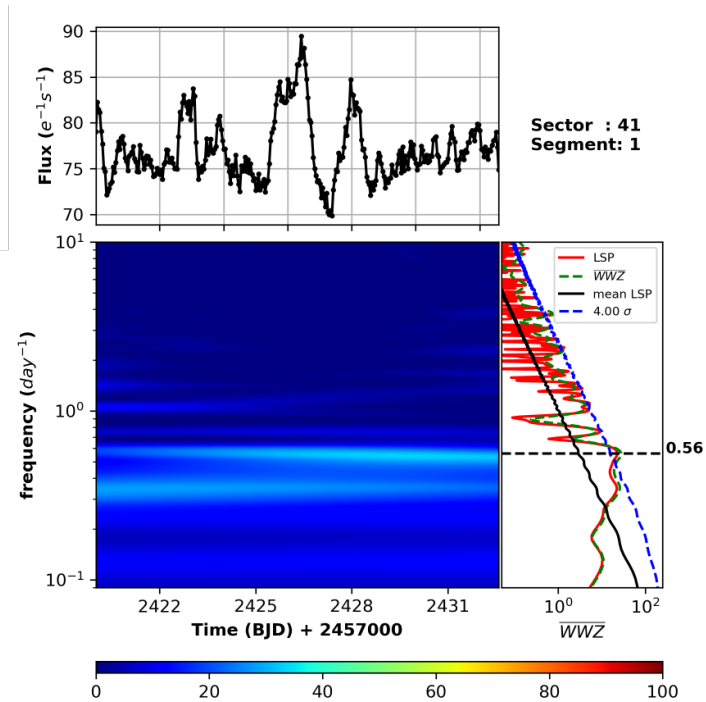


(b)

(H)



(a)



(b)

Fig. 6 continued..

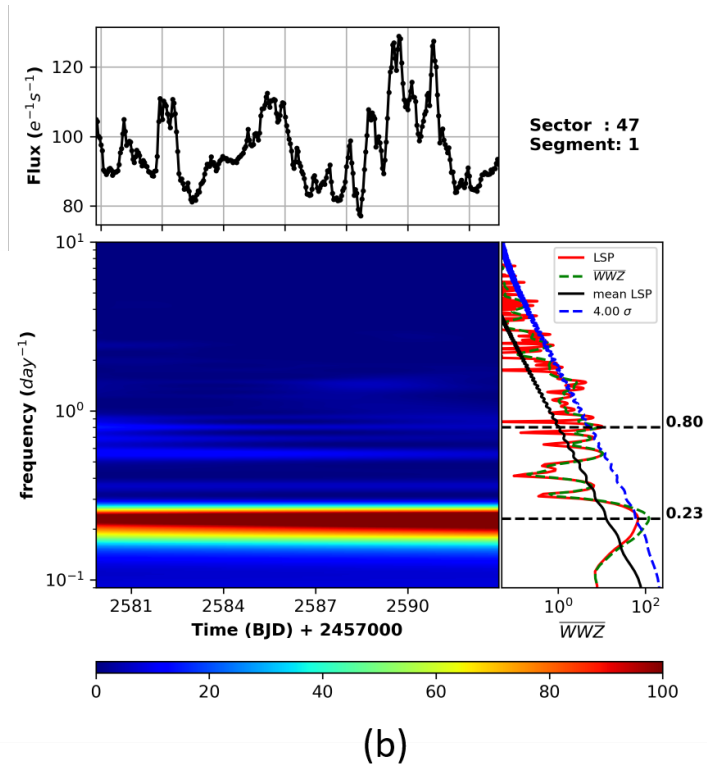
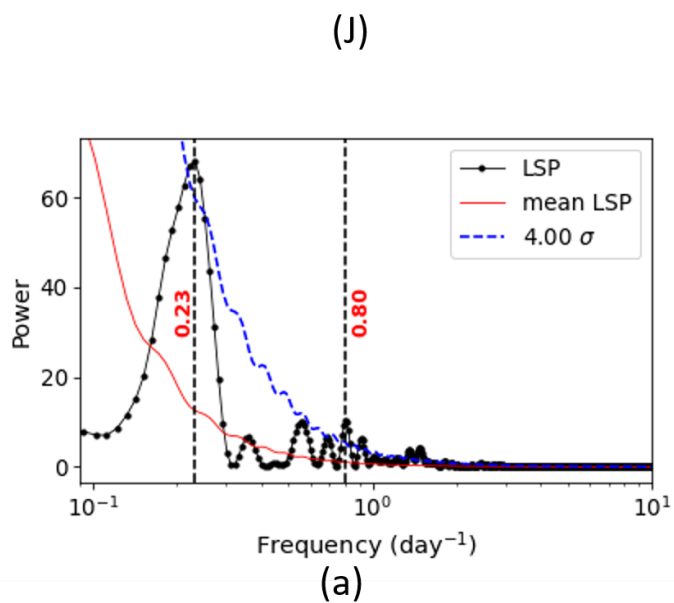
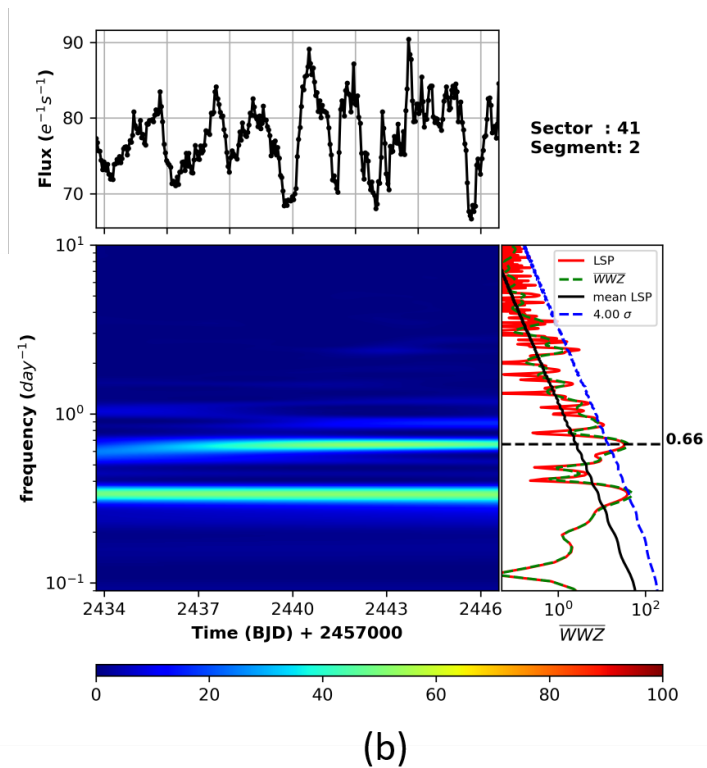
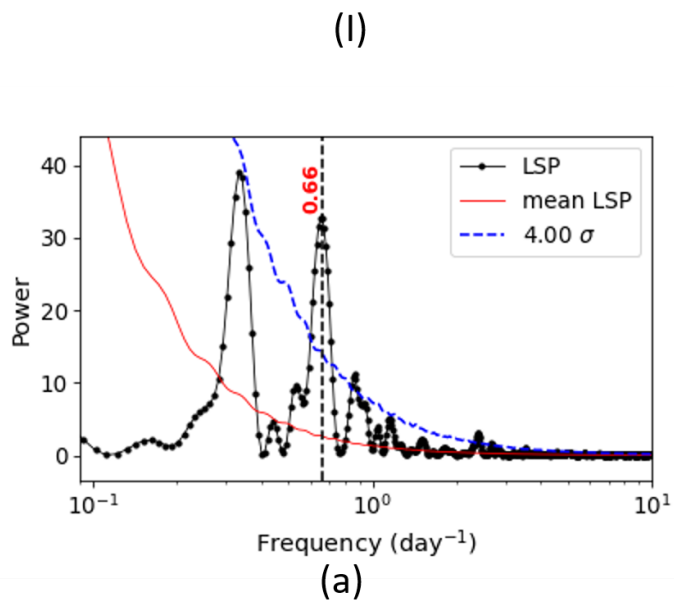
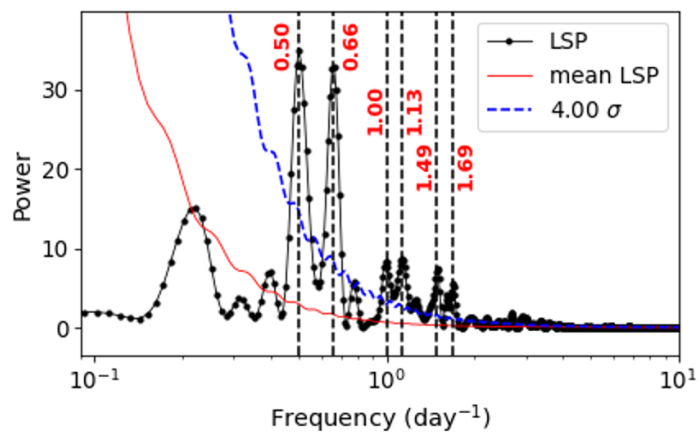
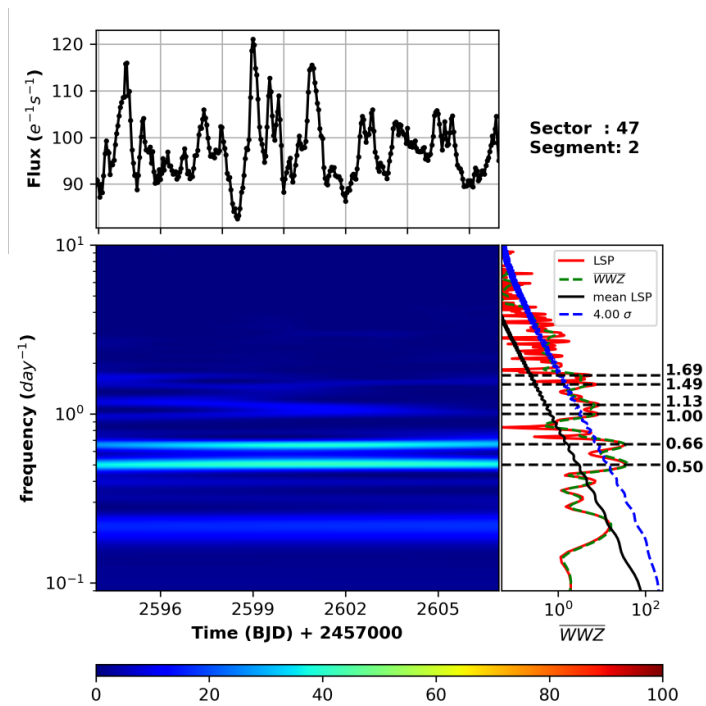


Fig. 6 continued..

(K)



(a)



(b)